nature communications

Article

https://doi.org/10.1038/s41467-025-57956-7

The structural diversity of psychedelic drug actions revealed

Received: 4 December 2024

Accepted: 6 March 2025

Published online: 19 March 2025

Check for updates

Ryan H. Gumpper[1,2,7] ✉, Manish K. Jain[1,7], Kuglae Kim[3], Renhong Sun[4], Ning Sun[4], Zhongli Xu[4], Jeffrey F. DiBerto[1,5], Brian E. Krumm[1], Nicholas J. Kapolka[5], H. Ümit Kaniskan[4], David E. Nichols[2], Jian Jin[4], Jonathan F. Fay[6] & Bryan L. Roth[1,2] ✉

There is currently a resurgence in exploring the utility of classical psychedelics to treat depression, addiction, anxiety disorders, cluster headaches, and many other neuropsychiatric disorders. A biological target of these compounds, and a hypothesized target for their therapeutic actions, is the 5-HT_{2A} serotonin receptor. Here, we present 7 cryo-EM structures covering all major compound classes of psychedelic and non-psychedelic agonists, including a β-arrestin-biased compound RS130-180. Identifying the molecular interactions between various psychedelics and the 5-HT_{2A} receptor reveals both common and distinct motifs among the examined psychedelic chemotypes. These findings lead to a broader mechanistic understanding of 5-HT_{2A} activation, which can catalyze the development of novel chemotypes with potential therapeutic utility and fewer side effects.

Over the past decade, classical psychedelics such as psilocybin, lysergic acid diethylamide (LSD), mescaline, and N,N-dimethyltryptamine (DMT) have been reexamined as potential therapeutics to treat various neuropsychiatric disorders[1–8]. Recently, psilocybin, the active ingredient in "magic-mushrooms" (*Psilocybe sp.*), was reported to be efficacious in multiple phase II clinical trials for the treatment of depression and anxiety[1]. Similarly, LSD, DMT, and mescaline have been reported to be potentially effective for treatment-resistant depression, alcohol and drug abuse, and various other neuropsychiatric conditions[5,6,8]. Intriguingly, the non-hallucinogenic LSD analog 2-bromo-LSD (BOL) was effective for cluster headaches in a small clinical trial[9].

Although the exact mechanisms responsible for psychedelic and therapeutic actions of these compounds are up for discussion, it is known that all classical psychedelics are 5-HT_{2A} serotonin (5-hydroxytryptamine; 5-HT) receptor (5-HT_{2A}R) agonists[10,11]. In addition, all psychedelic compounds exhibit complex polypharmacologies with potent interactions at many biogenic amine receptors[10]. However, even given the complex polypharmacology exhibited by most psychedelics, it is well-established that 5-HT_{2A}R agonism is responsible for the psychedelic effects in humans[12–15]. At the molecular level, there are currently two competing hypotheses on the mechanisms of psychedelic drug actions: (1) hallucinations arise from β-arrestin2 (βarr2) biased signaling at the 5-HT_{2A}R[10]; (2) there is a threshold of G-protein activation that will produce hallucinations and partial agonism below that will produce non-hallucinogenic 5-HT_{2A}R agonists[16]. From the neural circuit perspective, one hypothesis for the mechanism of the therapeutic effects of psychedelic drugs lies in their ability to induce the formation of spines and other measures of neuroplasticity in layer 5 pyramidal neurons[17–19] following a single administration. These findings are reminiscent of results from clinical trials on psilocybin, where a single dose was found to have anti-depressant effects lasting several months[4]. Although evidence has been steadily accumulating for the clinical use of psychedelics and the potential development of

[1]Department of Pharmacology, University of North Carolina at Chapel Hill School of Medicine, Chapel Hill, NC, USA. [2]Division of Chemical Biology and Medicinal Chemistry, Eshelman School of Pharmacy, University of North Carolina, Chapel Hill, NC, USA. [3]Department of Pharmacy, College of Pharmacy, Yonsei University, Incheon, Korea. [4]Mount Sinai Center for Therapeutics Discovery, Departments of Pharmacological Sciences, Oncological Sciences and Neuroscience, Tisch Cancer Institute, Icahn School of Medicine at Mount Sinai, New York, NY, USA. [5]EvE Bio, LLC, Durham, NC, USA. [6]Department of Biochemistry and Molecular Biology, University of Maryland Baltimore, Baltimore, MD, USA. [7]These authors contributed equally: Ryan H. Gumpper, Manish K. Jain. ✉e-mail: rgumpper@email.unc.edu; bryan_roth@med.unc.edu

novel 5-HT$_{2A}$R agonists, a fundamental understanding of the molecular interactions with the receptor is lacking. For example, the molecular interactions that participate in producing βarr2 biased signaling and partial agonism are currently unknown. Recently we published two 5-HT$_{2A}$R agonist structures with the N-benzylated phenethylamine 4-(2-((2-hydroxybenzyl)amino)ethyl)-2,5-dimethoxybenzonitrile (25CN-NBOH) and the ergoline LSD[20]. Even though that report represented a leap forward in the understanding of the structural biology of the 5-HT$_{2A}$R receptor, a clear gap remains in the elucidation of most 5-HT$_{2A}$R ligand interactions. Indeed, whereas crystal structures of 5-HT$_{2A}$R have been reported by others[21], they do not represent the canonical pose occupying the orthosteric site of the receptor (5-HT and psilocin) and contradict substantial biochemical and structural evidence.

Psychedelic 5-HT$_{2A}$R agonists are grouped into three basic chemotypes: tryptamines, ergolines, and phenethylamines (Fig. 1)[22]. Tryptamines closely resemble the native ligand 5-HT and include the psychedelics DMT, psilocin, and 5-methoxy-DMT, as well as non-psychedelic compounds, including melatonin and tryptophan. Ergolines contain a tryptamine core (Fig. 1) and are rigidified tetracycles derived from ergot alkaloids[22]. With LSD being one of the most potent psychedelics in the ergoline class, there are structural analogs such as 2-bromo-LSD (BOL) and lisuride, which are not hallucinogenic in humans[9,13]. Finally, phenethylamines resemble the neurotransmitter dopamine (Fig. 1) and exhibit a wide variety of potencies for the 5-HT$_{2A}$R[11,20]. Phenethylamines include compounds such as the classic psychedelic mescaline, which exhibits a low potency for 5-HT$_{2A}$R, as well as the potent and selective 5-HT$_{2A}$ agonist 25CN-NBOH[20].

In this work, to elucidate the structural details of psychedelic drug actions, we obtained seven cryo-EM structures of the 5-HT$_{2A}$R with representative compounds from each chemical class, including 5-HT, psilocin, DMT, mescaline, BOL, LSD, and a β-arrestin 2 (β-arr2) biased compound RS130-180 (Fig. 1). The structural characterization of this set of compounds (containing hallucinogenic/non-hallucinogenic and

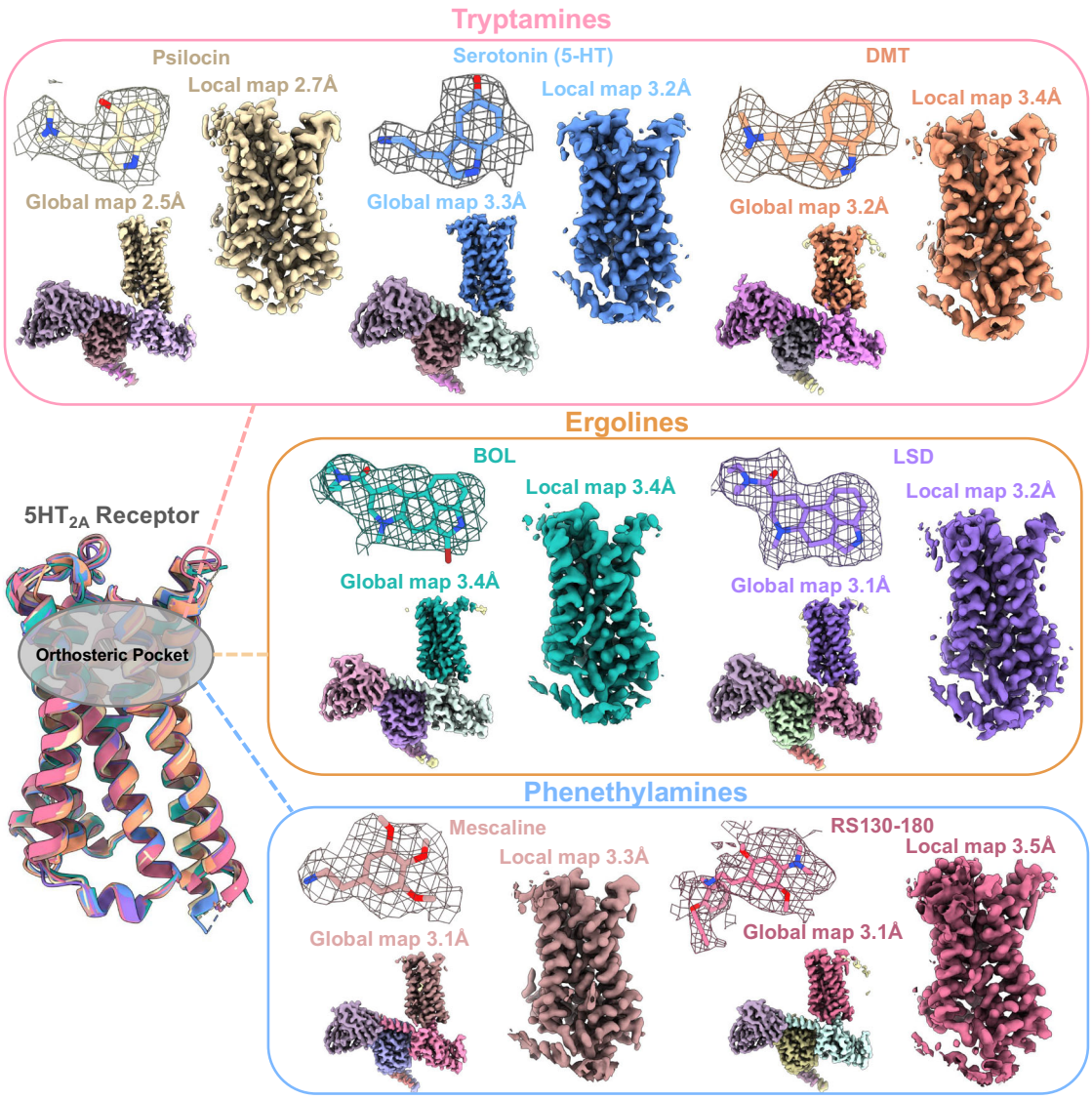

Fig. 1 | Cryo-EM Structures of the 5-HT$_{2A}$R with Various Psychedelic Ligands. All of the structures collected and analyzed in this work separated into the main ligand classes: tryptamines, ergolines, and phenethylamines. The local map, global map, ligand densities from the local map, and the resolution are given for each structure. All the maps shown were created from the half-maps utilizing deepEMhancer and the highRes model. However, the ligand densities are from the automatically sharpened output of the Local Refinement job in cryosparc. To maintain consistency, the receptor coordinates for both the global and local depositions remain identical and are modeled on the local refined map. All images were prepared using ChimeraX. The cartoon models shown in the bottom left represent all the receptors aligned to the 5-HT structure exhibiting the structural homogeneity between the ligands tested.

G-protein/β-arr2 biased compounds) allows us to propose several molecular mechanisms central to answering the outstanding questions of biased signaling, receptor selectivity, and partial agonism currently confounding the field of psychedelic science. Along with biochemical and pharmacological insights from these studies, we report how each class of ligands interacts with the 5-HT_{2A}R, leading to mechanistic insights useful for the development of novel psychiatric drugs.

Results

Structural elucidation of psychedelic drug interactions

To reveal the molecular determinants for psychedelic drug actions, we determined seven active state cryo-EM structures of the agonist-bound 5-HT_{2A}R in complex with heterotrimeric Gq. This set of structures contains ligands encompassing: (1) known psychedelic chemotypes (tryptamines, phenethylamines, and ergolines); (2) non-psychedelic analogs; and (3) a phenethylamine-derived β-arr2 biased agonist (Fig. 1). We utilized our previously employed construct for the 5-HT_{2A}R and previously designed mini-GαqiN-Gβ1-Gγ2 (mini-Gαq) heterotrimer with stabilizing single-chain antibody (scFv16) expressed in *Spodoptera frugiperda* (Sf9)[20]. For higher throughput structure determination, the complexes of receptor/heterotrimer were co-expressed, and purified[23,24]. Global reconstructions containing receptor, heterotrimer, and scFv16 were obtained for all the ligands tested (Supplementary Fig. 1A). However, due to the inherent flexibility of the receptor across the heterotrimer, the ligand density in the receptor portion of the reconstruction was occasionally inadequate for modeling (Supplementary Fig. 1A). Ligand densities were refined by performing a focused local refinement in cryoSPARC utilizing a loose mask (Supplementary Fig. 1A) around the receptor alone. In that way we obtained two maps for each structure: the first representing a global (receptor:heterotrimer complex) and the second representing local (receptor alone) reconstructions. We deposited maps and models with identical receptor coordinates based on the focused receptor refinement (Supplementary Fig. 1 and Supplementary Tables 1–4). For the tryptamines, we determined 5-HT (3.3 Å global and 3.2 Å local), psilocin (2.5 Å global and 2.7 Å local), and DMT (3.2 Å global and 3.4 Å local) (Fig. 1). For the ergolines we solved LSD (psychedelic) (3.1 Å global and 3.2 Å local) and 2-Br-LSD (non-psychedelic) (3.4 Å global and 3.4 Å local) (Fig. 1). Finally, for phenethylamines we resolved mescaline (3.1 Å global and 3.3 Å local) and the β-arr2 biased ligand RS130-180 (3.1 Å global and 3.5 Å local) (Fig. 1). All subsequent receptor-focused reconstructions allowed us to unambiguously model ligand densities as described here (Fig. 1, Supplementary Fig. 1A, C and Supplementary Table 1–4 for data collection and model statistics, and Supplementary Fig. 4) and resolution estimated by GSFSC (Gold Standard Fourier Shell Correlation) (Supplementary Fig. 2 and Supplementary Fig. 3). Importantly, ligand placements were verified by the Gemspot pipeline, a docking protocol that utilizes the cryo-EM map as restraints (Supplementary Fig. 1B)[25].

Despite the substantial chemical space that is recognized by the 5-HT_{2A}R, there is a remarkable global structural homology across the tryptamines, ergolines, and phenethylamines at the receptor level. Using the 5-HT:5-HT_{2A}R structure as a reference, a structural alignment yields a C-α RMSD of 0.6 Å for BOL, 0.6 Å for DMT, 0.6 Å for LSD, 0.5 Å for mescaline, 0.5 Å for psilocin, and 0.8 Å for RS130-180 (Fig. 1). We also compared our previously published 25CN-NBOH structure to the 5-HT structure and found it exhibits an RMSD of 1.0 Å (Fig. 1).

The tryptamine structures represent the canonical orthosteric pose

Examining the orthosteric site, all ligands make predicted receptor contacts and sit within a pocket defined by $D155^{3.32}$, $F339^{6.51}$, and $F340^{6.52}$, thereby validating more than 30 years of prior biochemical data and computational models for ligand interactions[20,22,26,27] (Figs. 2–4). Significantly, we find that psilocin interacts with the G protein-coupled state distinct from that recently proposed by another group for psilocin[21]. We also compared similar previously experimentally validated 5-HT receptor structures with our current structures (Supplementary Fig. 5). The 5-HT bound 5-HT_{1A}/5-HT_{1D} and the 5-CT bound 5-HT_{5A} structures were recently solved[26] by cryo-EM and aligning these with our structures, it is evident that the tryptamine substructure inhabits a similar position within the orthosteric pocket (Supplementary Fig. 5A). In addition, we compared the closely related 5-HT_{2C} receptor bound with psilocin[28] and our structure of psilocin bound to 5-HT_{2A}R. These structures exhibit significant overlap with the interacting residues in the orthosteric pocket, with psilocin exhibiting a small shift in the tryptamine core compared to the 5-HT_{2A} structure (Supplementary Fig. 5B). Thus, the overwhelming structural evidence across multiple serotonin receptor families suggests that the functionally active form of all examined tryptamine is in the validated orthosteric site and not in the recently hypothesized extended binding pocket (Supplementary Fig. 5C, D)[21].

To examine the key interacting residues within the orthosteric pocket for tryptamines, we quantified the differences in the contacts and validated the structural models by site-directed mutagenesis and subsequent functional assays (Supplementary Fig. 6 and Supplementary Table 5). First, we observed that 5-HT, psilocin, and DMT all make consistent ionic interactions with $D155^{3.32}$ and the primate-specific residue $S242^{5.46}$ as previously hypothesized, due to the similar positioning of the indole ring seen in other 5-HT_{2A} agonist structures[20,29]. However, when comparing the three tryptamines, we noted that there are slight shifts within the indole ring (Fig. 2A–C). Most notable is the change in the 4′-OH position of psilocin and the 5′-OH of 5-HT. The hydroxyl moiety on 5-HT sits within the H-bonding range with $N343^{6.55}$, whereas the psilocin hydroxyl group points towards the amino tail of the molecule (Fig. 2D). This finding is consistent with our mutagenesis studies where we found that the $N343A^{6.55}$ mutation influences 5-HT potency, suggesting electrostatic and/or potential water-mediated interaction between the endogenous ligand and $N343A^{6.55}$ (Supplementary Fig. 6 and Supplementary Table 5). However, that was not found with psilocin. DMT also shows a slight shift in the indole ring compared to 5-HT, as there is no accessory moiety on the indole ring to position the ligand (Fig. 2E).

Ergoline structures reveal a mechanism for 5-HT_{2A}R selectivity

The LSD analog BOL has been reported to be non-hallucinogenic in humans[9,13]. Previously, it was speculated that BOL acted as a 5-HT_{2A}R antagonist as reports of it being administered to humans in doses as high as 10 mg three times daily without any psychoactivity, whereas it subsequently blocked the hallucinogenic actions of LSD[30]. However, recapitulating recently published work, we found that BOL, instead, is a potent 5-HT_{2A}R G-protein biased partial agonist (Supplementary Fig. 13), which explains at least in part its ability to block the psychedelic actions of LSD in humans[31]. Within the orthosteric pocket, both ergolines make the expected hydrogen bonding contacts with $D^{3.32}$ and $S^{5.46}$ (Fig. 2F, G). BOL is especially intriguing as it differs by a single atom compared to LSD, bromine at the 2 positions (Figs. 1, 2F, G) and is non-hallucinogenic.

Comparing the binding poses of BOL with LSD in these structures, we observe that both ligands occupy similar binding positions (Fig. 2F, G). The most notable difference being the Br of BOL, which makes van der Waals contact with $I163^{3.40}$ deep within the orthosteric pocket and $F340^{6.52}$ (Fig. 2H). $I163^{3.40}$ is the I in the canonical PIF motif that undergoes a significant conformational change upon receptor activation, and interaction with this residue could potentially impede receptor activation resulting in weak-partial agonism. In addition, $F340^{6.52}$ is conserved throughout all 5-HT_2 family members and plays a universal role in ligand recognition[20]. When comparing our cryo-EM structures of 5-HT_{2A}-LSD and D_2-LSD (Fig. 2I), we observed significant overlap in the overall placement of the ligands. Also, we compared

https://doi.org/10.1038/s41467-025-57956-7

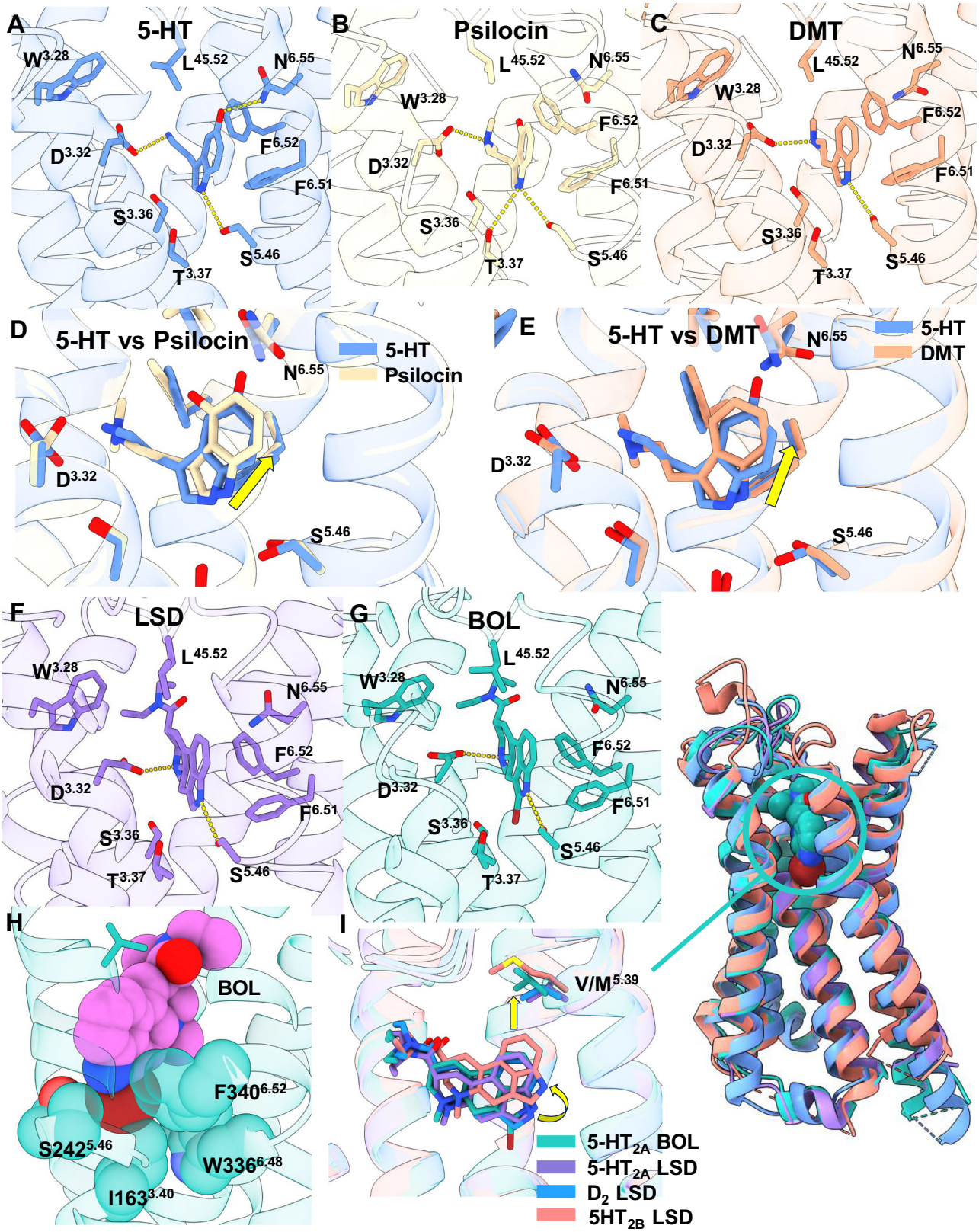

Fig. 2 | Receptor Ligand Interactions in the Orthosteric Pocket for Tryptamine and Phenethylamines. A–C Modeled interactions are shown by the dotted yellow line and based on the modeled distances from the cryo-EM structures. Each residue for the receptor is labeled by the Ballesteros–Weinstein (BW) numbering scheme. Each panel exhibits the structures: (**A**) 5-HT, (**B**) Psilocin, and (**C**) DMT. **D**, **E** Overlay of either 5-HT and Psilocin (**D**) or 5-HT and DMT (**E**). **F**, **G** Showcase the electrostatic interactions of either LSD (**F**) or BOL (**G**) shown in the dotted yellow line. **H** BOL and selected residues at the bottom of the orthosteric pocket shown as vdW spheres. **I** Overlay of 5-HT$_{2A}$R with either LSD or BOL from this work, 5-HT$_{2B}$R with LSD (PDB: 7SRQ), and D$_2$R LSD (PDB: 9BS9 (unpublished)).

these structures with our recently solved 5-HT_{2B}-LSD and the recently solved 5-HT_{1A}-LSD cryo-EM structures[32]. When aligning just the receptor portions of the complexes, we observed a considerable shift upward of the indole part of the ergoline ring (Fig. 2I and Supplementary Fig. 5F) for 5-HT_{2B}. This is due to two factors: (1) 5-HT_{2B} does not contain a serine at position 5.46 (it is an A) and loses the interaction with the indole N; and (2) the ring is pulled upwards through hydrophobic interactions with $M^{5.39}$ (Fig. 2I). At the 5.39 position in 5-HT_{2A}R, D_2R, and 5-HT_{1A}R, this is a valine, and in this regard, it was recently reported that BOL is a potent D_2R/5-HT_{1A}R agonist and a 5-HT_{2B} antagonist[31]. We hypothesize that BOL may also sit higher within the orthosteric pocket and act as an antagonist at 5-HT_{2B}, either potentially blocking the structural rearrangement of $I163^{3.40}$ or engaging these residues in a way that does not allow activation. This hypothesis was evaluated biochemically by testing reciprocal $V235M^{5.39}$/5-HT_{2A} and $M218V^{5.39}$/5-HT_{2B} mutations. Supporting this hypothesis, we found that switching these residues transforms BOL into a partial agonist at 5-HT_{2B} and greatly attenuates the potency and efficacy for BOL at 5-HT_{2A} (Supplementary Fig. 7 and Supplementary Table 6). Importantly, similar effects were not seen with LSD as it is not stabilized in this deep portion of the orthosteric pocket. This binding mode could, conceivably, be exploited as an approach for creating ergoline-based 5-HT_{2A} selective agonists through further exploration of the space deep within the orthosteric pocket.

Mescaline Interacts with the ECL2 Lid

The phenethylamines mescaline and RS130-180 exhibit similar binding poses (Fig. 3A, B and Supplementary Fig. 5E)[20]. Both mescaline and RS130-180 contact $D^{3.32}$ (Fig. 3A, B), whereas mescaline also contacts $S^{5.46}$ on helix 5 (Fig. 3A). Moreover, the mescaline-bound complex revealed a hydrophobic interaction with L229 on extracellular loop 2 (ECL2) through its 3'-position methoxy group (Fig. 3C). This interaction was previously found to be responsible for creating a lid on top of the orthosteric pocket with 5-HT_{2A} and 5-HT_{2B} LSD crystal structures to 'trap' LSD in the binding site[27]. This ECL2 lid was found to be responsible for LSD's long residence time on the receptor and, potentially, its extended duration of action[27]. In addition, L229 has a tight hydrophobic interaction with $F234^{5.38}$, which we hypothesized may be important for transmitting the signal through TM5 during receptor activation (Fig. 3C). Unexpectedly, the L229A mutant transformed mescaline from an agonist to an inverse-agonist (Fig. 3C). Furthermore, site-directed mutagenesis of $F234A^{5.38}$ showed that this residue is important for ligand-dependent activation of the receptor for both 5-HT and mescaline, indicating that stabilization of this residue is important for transmitting activation signals through TM5.

Because mescaline is stabilized by the same residue essential for LSD's prolonged receptor residence time, we wondered if the same process might apply to mescaline. As radioactive mescaline is not available, instead, we utilized a 5-HT_{2A}-κOR chimeric receptor and nanobody 6 (Nb6) pair to probe the conformational states of the receptor in a ligand-dependent manner as previously described[33]. We have previously characterized this Nb6 5-HT_{2A}-κOR chimera BRET pair and found it to be functionally relevant for 5-HT_{2A}R signaling[33]. This BRET-based assay affords us the ability to probe the active→inactive state transition and to compare the kinetics of ligand-stabilized conformations. Utilizing this technology, we probed 5-HT, mescaline, and LSD (Supplementary Fig. 8). After a baseline for 15 min, the agonist was added for a period of 50 mins. Immediately following agonist administration Nb6 dissociates from the inactive state consistent with an inactive→active state transition. After 50 min of agonist exposure, the potent 5-HT_{2A} antagonist risperidone (10 μM) was added, and the 5-HT and mescaline BRET response quickly returned to near basal levels. However, that is not seen with LSD similar to direct radioligand binding studies indicating a prolonged ligand residence time (and presumed long-term stabilization of the 'active' state)[27]. Our findings indicate that the closing of the ECL2 lid is essential for mescaline's interaction with L229 but that this interaction does not significantly modify apparent conformational transition kinetics. Furthermore, we examined all the ECL2 lids across all the structures and observed that they are closed (Supplementary Fig. 9) adding further evidence for the importance of this conformation in the transducer-coupled state. However, simple engagement with L229 may not drive dissociation kinetics for every class of compounds like it does with ergolines, but this has yet to be examined from the point of view of ECL2 loop dynamics.

A β-arrestin-biased 5-HT_{2A} agonist stabilizes a Non-canonical State

We next examined the binding mode of the βarrestin-2 biased N-benzylated phenethylamine, RS130-180 (see Supplementary Fig. 10 for NMR validation and Supplementary Fig. 11 for the synthetic scheme), which has shown utility as an in vitro tool compound, although it has suboptimal in vivo pharmacokinetic properties. RS130-180 was optimized for potency and bias from ZINC000341335936 ('5936), which was identified from a large-scale docking campaign[24]. One particularly interesting feature of the N-benzylated phenethylamines is their influence on the positioning of the "toggle-switch" tryptophan ($W^{6.48}$). Using the structural information from the 25CN-NBOH 5-HT_{2A}-Gq complex, we hypothesized that 'pushing' on the toggle switch was essential for its potency and efficacy[16,20]. However, this pushing on $W^{6.48}$ has not been replicated in any of the previously solved 5-HT_{2A} structures, including the ones in this work. To understand the potential structural features contributing to RS130-180's bias profile, and potential receptor changes during G-protein activation, we obtained a cryo-EM structure with RS130-180.

Like 25CN-NBOH, we found that RS130-180 directly interacts with $W^{6.48}$. However, due to the steric hinderance, and the additional bulk of RS130-180, the toggle switch adopts an *entirely downward facing position unseen in any reported 5-HT_{2A}R structures*. The displacement of $W^{6.48}$ causes an inward rotation of $F332^{6.44}$ (or the F in the PIF motif) towards the receptor core. This inward rotation of $F332^{6.44}$ pushes $Y380^{7.53}$ (Y of the NPxxY motif) outwards compared to the active state 5-HT structure and all other active state structures (Fig. 3D). We observed that this outward shift at the bottom of TM7 is reminiscent of the inactive state crystal[34](Fig. 3D). That creates a non-optimal conformation for G-protein activation as TMs 5 and 6 are in activate state conformations whereas TM7 is in an inactive state configuration. This type of intermediate state, the non-canonical (NC state), has been proposed through MD simulations and observed in recent structures[35,36]. To our knowledge, this represents the first occurrence in which the NC state is stabilized by an arrestin-biased ligand, as RS130-180 imperfectly stabilizes the Gq conformation, thereby favoring arrestin signaling and, perhaps, explaining the observed bias of the ligand.

Distinct ligand-stabilized conformational transitions

Examining the structural data in aggregate, we noticed distinct chemotype- and ligand-stabilized interactions based on the modeled coordinates. All ligands examined contact $D^{3.32}$, which is a long validated contact within the orthosteric pocket[20,24,27,32,37,38] (Fig. 4)(Supplementary Fig. 12 for interaction maps prepared by Maestro (Schrodinger)). Interestingly, 5-HT is the singular ligand in the structures that we solved that contacts $N^{6.55}$, and this contact could play an important role in 5-HT_2 family specific signaling as it is non-conserved throughout all 5-HT receptors. Another residue, $S^{5.46}$, which is unique to the primate 5-HT_{2A} receptor and not found in either the mouse or rat[20], interacts with all ligands examined, except for the N-benzylated phenethylamines 25CN-NBOH and RS130-180. In addition, psilocin was the only ligand to contact $T160^{3.37}$. $L229^{45.52}$ made hydrophobic contacts with DMT, mescaline, LSD, and BOL. Finally, a potential targeting mechanism for ergolines lies in $W151^{3.28}$ as both LSD and BOL were

https://doi.org/10.1038/s41467-025-57956-7

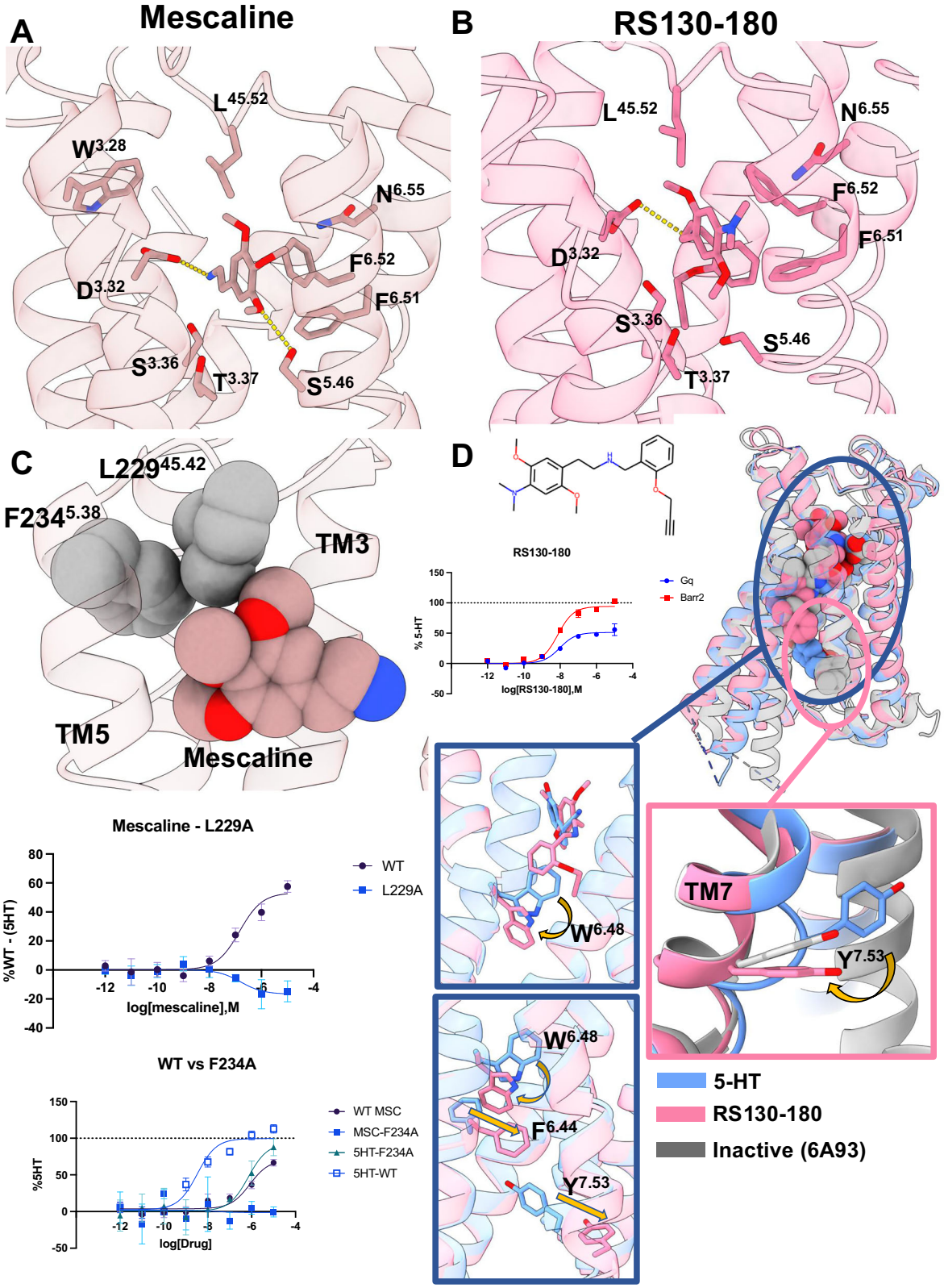

Fig. 3 | Molecular Interactions and Mechanisms of Phenethylamines. **A**, **B** Showcases the binding mode and modeled electrostatic interactions of mescaline (**A**) and the novel arrestin-biased compound RS130-180 (**B**). **C** Top panel shows the vdW sphere of mescaline and L229$^{45.52}$/F234$^{5.38}$. The bottom two panels indicate the TRUPATH assays and site-directed mutagenesis for each residue. Each point represents the mean ± SEM and $N = 3$ biological replicates. It is of note that the negative curve-fit shown in this panel is for visualization purposes of the inverse agonism only – no fit parameters were obtained from this fit. **D** Chemical representation of RS130-180. The top right panel represents the overlay of the 5-HT structure (blue), RS130-180 (pink), and an inactive state structure (gray, PDB ID: 6A93) as shown via cartoon representation. The dose-response curve for Gq (TRUPATH) and arrestin for RS130-180 showcases the arrestin bias of the compound. Each point represents the mean ± SEM and $N = 3$ biological replicates and is taken from the raw data in Supplementary Fig. 13 and Supplementary Table 8. The bottom portion is close-up panels showcasing the structural mechanism that RS130-180 utilizes to achieve its arrestin bias.

https://doi.org/10.1038/s41467-025-57956-7

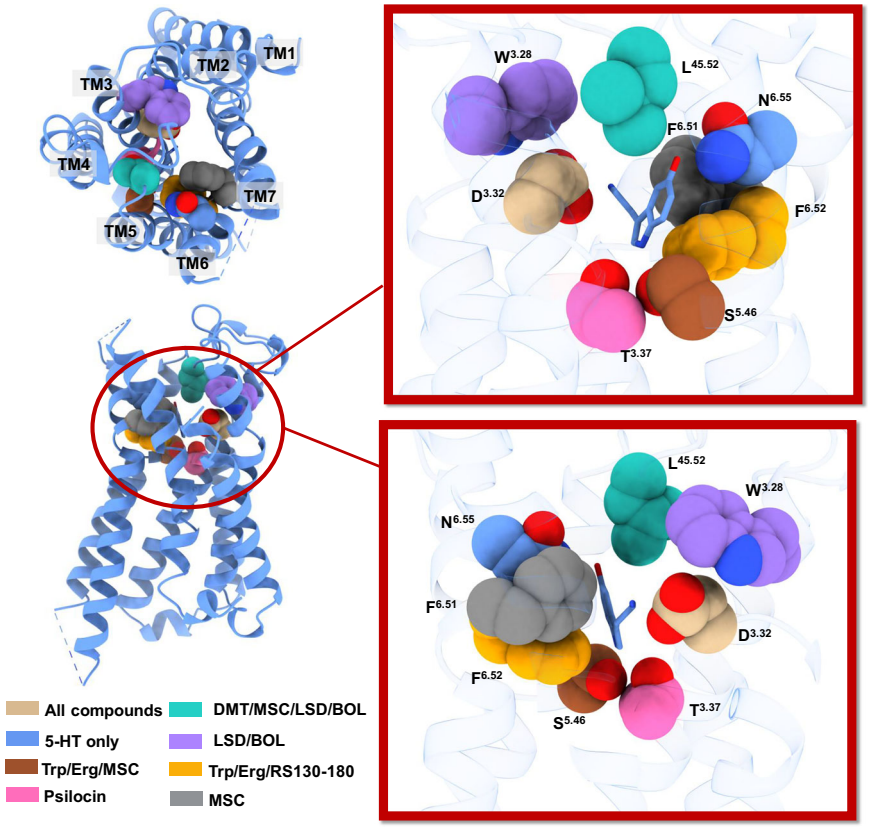

Fig. 4 | Aggregate Molecular Interactions. Selected important residues within the orthosteric pocket colored by their various selective properties across all the ligands examined in this study as well as two other active state structures. Each conglomerate of interactions is colored differently to indicate common/different interactions between chemotypes or individual compounds. Abbreviations are as follows: serotonin (5-HT), tryptamines (Trp), ergolines (Erg), 2-bromo-LSD (BOL), mescaline (MSC), 25CN-NBOH (NBOH), and N,N-dimethyltryptamine (DMT).

found to interact with this residue, whereas the other chemical classes do not. Finally, we validated long-proposed and important pi-stacking interactions in the orthosteric pocket[20,24,27,32,37,38] with F340$^{6.52}$ with all of the ligands except mescaline. However, mescaline does make a pi-cation interaction with the adjacent F339$^{6.51}$. These results reveal potential avenues for selective drug design by targeting various residues within the orthosteric pocket.

The finding that bias can arise in concert with observable conformational changes in 5-HT$_{2A}$ structures, as exemplified by the NC-state produced by RS130-180 in this work, led us to investigate the potential temporal effects of ligand bias. Figure 5A shows bias plots[39–41] as a function of time for all the ligands presented in this work and 25 CN-NBOH. To create these plots, dose-response curves utilizing our TRUPATH system (Gαq-heterotrimer dissociation) and β-arr2 recruitment were measured (see Supplementary Fig. 13 for dose-response curves and Supplementary Table 7 for fit parameters) in a time-dependent fashion. Interestingly, utilizing these assays we noticed that all the tested ligands exhibited Gαq bias except for RS130-180 and 25CN-NBOH. Both ligands are N-benzylated phenethylamines and directly interact with W336$^{6.48}$ (the "toggle switch"), causing a deviation in the tryptophan conformation compared to the other agonists, potentially revealing a mechanism for producing β-arr2 biased compounds. Subsequently, we noticed that the G-protein signaling for both compounds catches up at later time points as the plots move towards "even" signaling, suggesting a kinetic component to this type of bias. It was previously shown in D2R that ligand binding kinetics can modulate signaling bias through receptor occupancy time – i.e., the longer the ligand activates the receptor, the longer all the various signal transduction pathways can be activated in the system, leading to changes in bias in a time-dependent manner[42]. However, due to both RS130-180 and 25CN-NBOH molecularly targeting the important toggle switch residue (W336$^{6.48}$), which is important in modulating inactive→active state transition, we hypothesized that the observed bias is being achieved through a conformational stabilization of the receptor and not the ligand binding kinetics. To probe both ligand dissociation and the potential inactive→active state conformational transitions we utilized the 5-HT$_{2A}$-κOR and Nb6 BRET pair against the remaining ligands as well as 25CN-NBOH. We found that both 25CN-NBOH and RS130-180 dissociated rapidly from the receptor after the addition of risperidone (Supplementary Fig. 14), unlike the ergolines LSD and BOL, suggesting shorter receptor occupancy times. This would indicate that in the case of 25CN-NBOH and RS130-180, the change in the observed signaling bias is not due to ligand kinetics, but through the stabilization of a specific conformational state of the receptor, which in turn modulates the kinetics of the activation/recruitment of the transducer.

In addition, we observed that several agonists induce different maximal responses when compared to other BRET probes (i.e., β-arr2 recruitment or heterotrimer dissociation) (Fig. 5C). To best compare % activation of these three datasets, we matched them for time (in this case ~ 55 min for Nb6 or 60 min for Gq/β-arr2) and ligand concentration. In examining this plot, we noticed that the NB6 response for all compounds closely mimicked the β-arr2 response, except for LSD (Fig. 5C, Supplementary Fig. 8, and Supplementary Fig. 14). In addition, both the N-benzylated phenethylamines (25CN-NBOH and RS130-180) showed a larger response than the β-arr2 response. Because Nb6 is sensing the inactive→active state transition, the variances in maximal responses suggest a fundamental difference in how each ligand stabilizes this conformational transition (Fig. 5B). This corroborating

https://doi.org/10.1038/s41467-025-57956-7

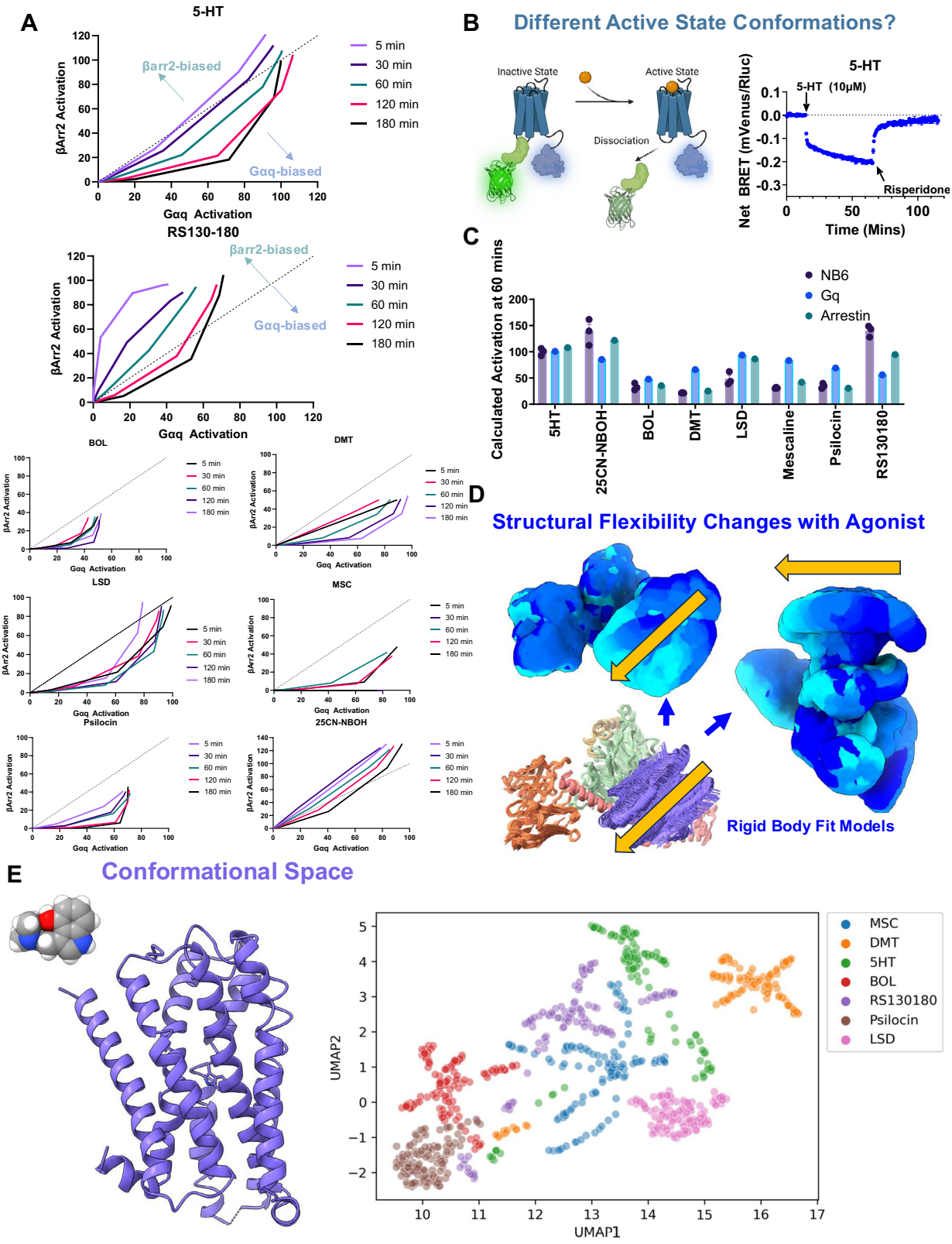

biochemical evidence from the structural data further suggests these compounds adopt distinct conformational states upon ligand activation, leading to their signaling behaviors.

To explore the features of the different conformational transitions observed by the ligand-dependent NB6 dissociation, we examined the observable structural distributions available to us in our cryo-EM ensembles (Fig. 5D, E and Supplementary Fig. 15). Although we acknowledge that a cryo-EM structure is an average of many microstates, analyzing the distribution of conformations is informative. In addition, we also realize that these structures do not utilize the native Gαq as a transducer, which may bias conformations of the receptor, but it should be noted that the use of mini-Gαq does not change the efficacy/potency of 5-HT_{2A}R signaling. Unlike 3DVA[43], in which each particle represents the linear combination of the latent space

Fig. 5 | Differences in Signaling Reveal Distinct Conformational States of Psychedelics. A Bias plots (Gq activation vs β-arr2 activation) from the time course seen in Supplementary Fig. 13 and Supplementary Table 8. **B** Cartoon of Nb6 dissociation and the time course of 5-HT. Data represent $N = 3$ biological replicates and mean ± SEM. Created in BioRender. Gumpper, R. (2025) https://BioRender.com/u71s141 (**C**) The calculated activation of each signaling assay matched for time (55 mins for Nb6 and 60 min for Gq/β-arr2) and concentration. For the NB6 assays, this data represents $N = 3$ biological replicates. For Gq/β-arr2, the calculated activation is based on the fit parameters at 60 minutes and matched for concentration. These fit parameters can be found in Supplementary Fig. 13 and Supplementary Table 8, where the number of biological replicates is also recorded. **D** Workflow of the output from cryoSPARC 3DFlex to generate models for downstream analysis and dimensionality reduction. **E** Aggregate data of the flexibility analysis using the Flex-refine protocol in cryoSPARC reveals conformational selectivity of the ligands. This is a UMAP of the models derived from the maps output by 3DFlex. Each color represents a different ligand, and abbreviations are as follows: mescaline (MSC), N,N-dimethyltryptamine (DMT), serotonin (5HT), 2-bromo-LSD (BOL).

component, 3DFlex[44] models the deformation flow field of the consensus map in a nonlinear fashion, capturing more information about the overall movement of the conformational ensemble of the particle stack. Once the ensemble of maps was generated, we used phenix.refine[45] and did two rounds of rigid body refinement into the maps. We observed that all structures contained conformational "rocks" and "twists," as has been reported for other GPCRs[43]. However, each structure exhibited distinct patterns of these "rocks" and "twists" containing ligand-dependent variations in both the direction and magnitude (Supplementary Fig. 15). Importantly, both the direction and magnitude of the "rock" and "twist" patterns were not affected by the size of the dataset as the 5-HT-complexes exhibited large movements (~157 K particles) whereas BOL (~603 K particles) was relatively stable. To compare the high-dimensional structural information, we employed dimensionality reduction (UMAP[46]) (Fig. 5E). Remarkably, despite aligning all structures before dimensionality reduction, each ligand stabilizes distinct conformational spaces (Fig. 5E).

Discussion

The cryo-EM structures presented represent the known agonist classes related to psychedelic drug action at the 5-HT_{2A}R. Utilizing this structural information will lead to insights into structure-aided drug design for novel psychedelic therapies. Although the exact mechanisms of action of psychedelic drugs are still unknown, this work represents a leap forward in the molecular understanding leading to this phenomenon. This work provides several mechanistic breakthroughs in understanding 5-HT_{2A}R actions by various psychedelics: mescaline interacts with the ECL2; a method for designing ergoline-based compounds for 5-HT_{2A} selectivity over 5-HT_{2B} revealed by the non-hallucinogenic BOL; a potential mechanism of partial agonism through BOL targeting $I^{3.40}$ a key molecular switch (PIF-motif) for class A GPCR activation, and validation that targeting $W^{6.48}$ (toggle switch) by N-benzylated phenethylamines produces arrestin biased compounds through modulation of receptor structure. Moreover, we have observed that different agonists stabilize varying conformational ensembles of the receptor coupled to the active-state heterotrimer.

Due to a recent resurgence in interest for utilizing psychedelic compounds as intermittently dosed therapeutics to treat depression, anxiety, addiction, cluster headaches, and many other neuropsychiatric disorders[2–6,8,9] it essential that we understand the details of action for these historically ostracized compounds. This study reveals the molecular underpinnings of ligand-receptor interactions while offering insights that will accelerate the pursuit of safer psychiatric therapeutics.

Methods

Expression and Purification of scFv16

The expression and purification of scFv16 was carried out as described previously[47]. In short, Sf9 cells were infected with an MOI of 3. 96 h post-infection (hpi) the cells were centrifuged at 3000 × *g* for 15 min. The supernatant media was collected, and the pH was adjusted to 7.8 using a Tris base. Chelating agents in the media were quenched with the addition of 1 mM $NiCl_2$ and 5 mM $CaCl_2$ and allowed to stir for 1 hr at RT. The precipitants were removed by additional centrifugation. After centrifugation, 1-2 mL of His60 Ni Superflow Resin was added to the media and allowed to stir overnight at 4 °C. The resin is collected the next day and washed with 20 CV of 20 mM HEPES pH 7.5, 500 mM NaCl, and 10 mM imidazole. The protein is then eluted with 20 mM HEPES pH 7.5, 100 mM NaCl, and 250 mM imidazole. The protein is then concentrated for further purification using a Superdex 200 16/60 column (GE). The peak fraction is collected/concentrated and stored at 4 °C or flash frozen to be kept in the − 80 °C for future use.

Expression and Purification of 5-HT_{2A}R-miniGq complex

All constructs used in a complex generation were published in our previous structural work on the 5-HT_{2A}R[20,23]. An MOI of 3 (5-HT_{2A}R receptor) and an MOI of 1.5 (miniGq heterotrimer) was used to infect Sf9 cells. 48 hpi cells were harvested through centrifugation at 3000 × *g* for 15 min and washed with HN buffer (20 mM HEPES pH 7.4, 100 mM NaCl), and stored at − 80 °C until purification. Cells were thawed on ice and incubated with a buffer containing 20 mM HEPES pH 7.5, 50 mM NaCl, 1 mM MgCl2, 2.5 units of Apyrase, proteinase inhibitors (500 µM AEBSF, 1 µM E-64, 1 µM Leupeptin, 0.15 µM Aprotonin), and between 5–50 µM of ligand of choice at RT on a rotator. After 2 hr, the cell suspension was dounce homogenized, and membranes were collected by centrifugation at 30,000 rpm (71,000 × *g*) for 30 min (Ti45 rotor). The membrane pellet was collected and solubilized in 40 mM HEPES pH 7.5, 100 mM NaCl, 5% (w/v) glycerol, 0.06% cholesteryl hemisuccinate (CHS), 0.6% lauryl maltose neopentyl glycol (LMNG), 500 µg of scFv16 purified protein, and between 5–50 µM ligand of choice for 5 hr at 4 °C. The solubilized lysate was clarified through centrifugation for 1 hr at 60,000 rpm (264,000 × *g*) at 4 °C (Ti70 rotor). 20 mM imidazole and 2.5 µL of PNGaseF was then added to the supernatant and incubated overnight at 4 °C with Talon IMAC resin. The next day the resin was collected and washed with 25 CV of 20 mM HEPES pH7.5, 100 mM NaCl, 30 mM imidazole, 0.01% (w/v) LMNG, 0.001% (w/v) CHS, with 5–50 µM of ligand of choice, and 5% glycerol. The protein was then eluted with the same buffer but with 250 mM imidazole. After elution, the protein was immediately concentrated and subjected to SEC (Superose 6 equilibrated 20 mM HEPES pH 7.5, 100 mM NaCl, 100 µM TCEP, 0.00075% (w/v) LMNG, 0.00025% (w/v) glycol-diogenin (GDN), 0.00075% CHS, and 5–50 µM ligand of choice). The appropriate peak fractions were collected and subjected to cryo-EM analysis. The protein was then concentrated to 3–5 mg/mL, and an additional 5–50 µM of ligand is added and allowed to incubate for 1-2 hr before making grids.

Cryo-EM Sample preparation, data collection and processing

Quantifoil R 1.2/1.3 Au 300 holey carbon film grids were glow discharged and individually frozen in a 60/40 ethane propane mixture using a Vitrobot mark IV (FEI). The blot time of each grid ranged from 2.5–5 s with the humidity set to 95% at 4 °C. All images were collected on a 200 keV G3 Talos Arctica with a Gatan K3 direct electron detector with a pixel size of 0.88 Å for ~ 2.7 seconds for 60 subframes with a total exposure of ~ 50 electrons/ $Å^2$. A multi-shot array utilized and recorded automatically using SerialEM[48]. The micrographs were manually curated, inspected, and processed using cryoSPARC v3.1 or v4.1[49,50]. All data collection statistics and example processing tree can

be found in Supplementary Fig. 1 and Supplementary Tables 1–4. The processing tree is like our previously published structures[20,23,37,51]. A gold-standard Fourier shell correlation cutoff of 0.143 Å was used to determine global resolution[52,53]. The maps and models were validated through using the half-maps and B-factor sharpened maps using Mtriage in the Phenix Software package[54–56]. To assist visualization of the maps in Fig. 1, alternative sharpening was performed on the half-maps using deepEMhancer[57]. Other than the densities shown in Fig. 1 for visualization purposes, only the automatically sharpened maps that are output from cryoSPARC non-uniform refinement or local refinement jobs were deposited and used for model building and subsequent structural analysis.

Model building and refinement

The initial model for each structure was derived from our previously published structure coordinates from PDB 6WHA[20]. Initial placement of the complex was done using the fit-to-map function in ChimeraX[58]. The model was then subjected to Phenix Real-space refinement with a rigid body turned on for a single round. Further modeling and structure validation was done using COOT, with a final round of refinement model cleanup done using the ChimeraX plugin ISOLDE and COOT[59,60]. For ligands that did not already have restraints deposited in the PDB, they were generated using Phenix Elbow[61]. The final model was further validated using Phenix Mtriage to examine the map-to-model quality and model statistics were generated by MolProbity[56]. All the structure figures were generated using ChimeraX[58]. Model statistics can be found in Supplementary Tables 1–4.

Structural flexibility analysis

To capture potentially non-linear and complex motions of the receptor-heterotrimer, we utilized cyroSPARC's 3DFlex pipeline to generate the conformational landscape from each set of particles[44]. Uniformly, each dataset was down-sampled 4.3 x (i.e., from a box size of 312 pixels to 72 pixels) during the 3D-Flex preparation step. For the flex-mesh preparation, the mask was set to a level to exclude the micelle, while keeping the protein parts. During Flex training 3 latent dimensions were used, and the centering strength was adjusted to make sure that all particles stayed with −1.5 to 1.5 across the 3 latent dimensions. Finally, Flex Generate was used to output 41 frames per latent dimension for a total of 123 reconstructions per structure. To fit models to begin a more in-depth structural analysis, 6WHA was used to be manually fit into the first frame by ChimeraX[58]. Utilizing phenix.refine the same model was then fit into each frame via 2 cycles of rigid body refinement[54]. All of these PDBs were then input as trajectories into MDAnalysis[62], and every structure was aligned to the original 5-HT structure. From here, UMAP was carried out using only the Cαs. All plots shown were done in matplotlib and Seaborn.

TRUPATH assays (BRET2)

The TRUPATH (BRET2) assays were carried out[63]. Briefly, 2 hrs prior to transfection in 10 cm dishes media was replaced with DMEM containing 1% dialyzed FBS. A ratio of 1:1:1:1 of receptor:Gα:Gβ:Gγ with 1 µg of each plasmid was transfected using Transit 2020 (Mirus Biosciences) following the manufacturers protocol. The next day the cells were plated into poly-L-lysine coated 96-well plates at a concentration of 40–50 k cells per well in DMEM containing 1% dialyzed FBS. 48 h post-transfection, the media was removed from the 96 well plates and covered with 60 µL of assay buffer (1x HBSS, 20 mM HEPES pH 7.4) and allowed to incubate at 37 °C for 10 minutes. After the incubation of 30 µL of 3X drug binding buffer (1X HBSS, 20 mM HEPES pH 7.4, 0.3% (w/v) BSA, 0.03% (w/v) Ascorbic Acid, ligand to be tested) was added and allowed to incubate for 10 min at RT. For specific kinetic assays the ligand was allowed to incubate with the cells for the listed amount of time before reading. Coelenterazine 400a was added to each well, followed by an additional 10-minute incubation. The BRET ratio was read (395 nm/510 nm) on a PHERAstar FSX for a total of 5 scans. The final read was taken for each plate for further analysis.

β-arrestin Recruitment assays (BRET1)

The β-arrestin recruitment assays were carried out using the same protocol as mentioned for the TRUPATH assays above, except a 1:2.5:5 ratio of receptor:GRK2:β-arr2 was used during transfection, and coelenterazine H was used as the *R*Luc substrate. For the kinetic time point assay, each ligand was incubated with the cells for that specific amount of time before reading.

Nb6 Dissociation from 5-HT_{2A}-κOR chimera

Utilizing the previously made and optimized constructs, the κOR ICL3 was inserted into the ICL3 of 5-HT_{2A}[33]. This allows for Nb6 binding and acts as a conformational sensor for inactive/active states, as previously shown[33]. HEK293T cells were co-transfected and plated similarly to the BRET2 assays but with the chimeric 5HT_{2A}-κOR-Rluc and Nb6-mVenus ratio 1:5, respectively. Kinetic traces were recorded on the Pherastar FSX for a total of 120 minutes every 30 s: 15 mins for baseline, 50 mins with agonist addition, and 55 mins with 10 µM antagonist (risperidone) addition using BRET1 plus optic module.

General chemistry methods

All commercial chemical reagents and solvents were used for the reactions without further purification. Flash column chromatography was performed on a Teledyne ISCO CombiFlash Rf+ instrument equipped with a 220/254/280 nm wavelength UV detector and a fraction collector. Normal phase column chromatography was conducted on silica gel columns with either hexane/ethyl acetate or dichloromethane/methanol as eluent. All final compounds were purified with preparative high-performance liquid chromatography (HPLC) on an Agilent Prep 1200 series with the UV detector set to 220/254 nm at a flow rate of 40 mL/min. Samples were injected onto a Phenomenex Luna 750 × 30 mm, 5 µm C18 column, and the gradient was set to 10% of acetonitrile in H_2O containing 0.1% TFA progressing to 100% of acetonitrile. For chiral separation, a Lux R 5 µM i-Amylose-3 column was used and samples were separated with preparative high-performance liquid chromatography (HPLC) on an Agilent Prep 1200 series with the UV detector set to 220/254 nm at a flow rate of 40 mL/min (method: solvent: H_2O (0.1% TFA): CH_3CN, 0 – 30 min (90% :10% - 0%: 100%), 30 min – 35 min (0%: 100%). All final compounds prepared had purity > 95% as determined by an Agilent 1200 series system with a DAD detector and a 2.1 mm × 150 mm Zorbax 300SB-C18 5 µm column for chromatography and high-resolution mass spectra (HRMS) that were acquired in positive ion mode using an Agilent G1969A API-TOF with an electrospray ionization (ESI) source. Samples (2 µL) were injected onto a C18 column at room temperature, and the flow rate was set to 0.4 mL/min with water containing 0.1% formic acid as solvent A and acetonitrile containing 0.1% formic acid as solvent B. Nuclear magnetic resonance (NMR) spectra were acquired on Bruker DRX 400 MHz for proton (^{1}H NMR) and 101 MHz for carbon (^{13}C NMR). Chemical shifts for all compounds are reported in parts per million (ppm, δ). The format of the chemical shift was reported as follows: chemical shift, multiplicity (s = singlet, d = doublet, t = triplet, q = quartet, m = multiplet), coupling constant (J values in Hz), and integration. All final compounds had > 95% purity using the HPLC methods described above.

Synthetic procedure for the synthesis of 2,5-dimethoxy-*N*,*N*-dimethyl-4-(2-((2-(prop-2-yn-1-yloxy)benzyl)amino)ethyl)aniline (RS130-180)

To a solution of commercially available 2,5-dimethoxy-*N*,*N*-dimethylaniline (**1**) (400 mg, 2.2 mmol) in acetone (5 mL) was added *N*-bromosuccinimide (NBS) (431 mg, 2.42 mmol, 1.1 equiv). The resulting suspension was stirred at 0 °C for 2 h. The reaction mixture was

concentrated and purified by flash chromatography (hexane / ethyl acetate = 10:1 to 3:1) to afford 4-bromo−2,5-dimethoxy-*N*,*N*-dimethylaniline (**2**) as a yellow solid (464.1 mg, yield 82%). Intermediate **2** (464.1 mg, 1.78 mmol) was then dissolved in toluene (6 mL) and water (3 mL), then (2-((*tert*-butoxycarbonyl)amino)ethyl)trifluoroborate potassium (670 mg, 2.67 mmol, 1.5 equiv), $Pd(OAc)_2$ (40 mg, 0.178 mmol, 0.1 equiv), Ruphos (166 mg, 0.356 mmol, 0.2 equiv), and cesium carbonate (1.74 g, 5.34 mmol, 3 equiv) were added. The reaction mixture was stirred at 110 °C overnight. The reaction mixture was then cooled to room temperature, and extracted with ethyl acetate, washed with brine, dried over Na_2SO_4, filtered, and then evaporated. The residue was purified by flash chromatography (hexane/ethyl acetate = 3:1 to 1:1) to afford *tert*-butyl (4-(dimethylamino)-2,5-dimethoxyphenethyl)carbamate (**3**) as a yellow solid (510 mg, yield 88%). To a solution of compound **3** (150 mg, 0.46 mmol) in DCM (1 mL) was added TFA (1 mL). The resulting suspension was stirred at rt for 1 h. The resulting mixture was concentrated and purified by reverse phase column (10%–100% acetonitrile/ 0.1% TFA in H_2O) to afford 4-(2-aminoethyl)-2,5-dimethoxy-*N*,*N*-dimethylaniline (**4**) as a yellow oil (100 mg, yield 97%). To a solution of compound **4** (100 mg, 0.45 mmol) in methanol (1 mL) were added commercially available 2-(prop-2-yn-1-yloxy)benzaldehyde (**5**) (71.4 mg, 0.45 mmol, 1 equiv), Et_3N (5 drops) and AcOH (10 drops), the mixture was stirred for 1 h at rt, then sodium cyanoborohydride (84.1 mg, 1.3 mmol, 3 equiv) was added. The resulting mixture was stirred at rt for 1 h. The mixture was filtered through celite. The resulting mixture was purified by prep-HPLC (10% – 100% acetonitrile/ 0.1% TFA in H_2O) to afford the final compound in TFA salt form (121 mg), then added 1 mL saturated $NaHCO_3$ solution, extracted with ethyl acetate, washed with brine, dried over Na_2SO_4, filtered, and evaporated. Then added 1 equiv. HCl.dioxane (4 N solution, 50 µL), and stirred at rt for an additional 1 h. The reaction mixture was then concentrated and the residue lyophilized to afford 2,5-dimethoxy-*N*,*N*-dimethyl-4-(2-((2-(prop-2-yn-1-yloxy)benzyl)amino) ethyl)aniline (**RS130-180**) as a light yellow solid (81 mg, 2HCl salt, yield 41%). ^{1}H NMR (400 MHz, methanol-d_4) δ 7.46 (q, J = 7.6, 6.8 Hz, 2H), 7.36 (d, J = 4.3 Hz, 1H), 7.24 (t, J = 4.1 Hz, 2H), 7.09 (d, J = 6.7 Hz, 1H), 4.91 (t, J = 3.3 Hz, 2H), 4.30 (s, 2H), 4.01 (s, 3H), 3.91 (s, 3H), 3.29-3.26 (m, 8H), 3.11-3.06 (m, 3H). ^{13}C NMR (101 MHz, MeOD) δ 156.02, 152.13, 144.66, 131.60, 131.15, 129.45, 127.91, 121.51, 119.48, 115.51, 112.39, 103.92, 77.90, 76.42, 56.23, 55.76, 55.70, 46.22, 46.16, 44.99, 26.88. HRMS (m/z) for $C_{22}H_{29}N_2O_3^+$ $[M+H]^+$: calculated 369.2173, found 369.2171.

Reporting summary

Further information on research design is available in the Nature Portfolio Reporting Summary linked to this article.

Data availability

All maps and coordinates have been deposited in the PDB and EMDB. The accession numbers/codes (PDB/EMDB-ID) are as follows: 5-HT2A-miniG_q-5-HT local (9ARX /EMD-43797), 5-HT2A-miniG_q-5-HT global (9ARY/EMD-43798), 5-HT2A-miniG_q-BOL local (9ARZ/EMD-43799), 5-HT2A-miniG_q-BOL global (9AS0/EMD-43800), 5-HT2A-miniG_q-DMT local (9AS1/EMD43801), 5-HT2A-miniG_q-DMT global (9AS2/EMD-43802), 5-HT2A-miniG_q-LSD local (9AS3/EMD-43803), 5-HT2A-miniG_q-LSD global (9AS4/EMD-43804), 5-HT2A-miniG_q-mescaline local (9AS5/EMD-43805), 5-HT2A-miniG_q-mescaline global (9AS6/EMD-43806), 5-HT2A-miniG_q-psilocin local (9AS7/EMD-43807), 5-HT2A-miniG_q-psilocin global (9AS8/EMD-43808), 5-HT2A-miniG_q-RS130-180 local (9AS9/EMD-43809) 5-HT2A-miniG_q-RS130-180 global (9ASA/EMD-43810). Source data are provided in this paper.

References

1. Carhart-Harris, R. et al. Trial of psilocybin versus escitalopram for depression. *N. Engl. J. Med.* **384**, 1402–1411 (2021).
2. Carhart-Harris, R. L. et al. Psilocybin with psychological support for treatment-resistant depression: an open-label feasibility study. *Lancet Psychiatry* **3**, 619–627 (2016).
3. Griffiths, R. R. et al. Psilocybin produces substantial and sustained decreases in depression and anxiety in patients with life-threatening cancer: A randomized double-blind trial. *J. Psychopharmacol.* **30**, 1181–1197 (2016).
4. Carhart-Harris, R. L. et al. Psilocybin with psychological support for treatment-resistant depression: six-month follow-up. *Psychopharmacology* **235**, 399–408 (2018).
5. Fuentes, J. J., Fonseca, F., Elices, M., Farré, M. & Torrens, M. Therapeutic use of LSD in psychiatry: A systematicreview of randomized-controlled clinical trials. *Front. Psychiatry* **10**, 943 (2019).
6. Agin-Liebes, G. et al. Naturalistic use of mescaline is associated with self-reported psychiatric improvements and enduring positive life changes. *ACS Pharmacol. Transl. Sci.* **4**, 543–552 (2021).
7. Ley, L. et al. Comparative acute effects of mescaline, lysergic acid diethylamide, and psilocybin in a randomized, double-blind, placebo-controlled cross-over study in healthy participants. *Neuropsychopharmacology* **48**, 1659–1667 (2023).
8. Garcia-Romeu, A. et al. Cessation and reduction in alcohol consumption and misuse after psychedelic use. *J. Psychopharmacol.* **33**, 1088–1101 (2019).
9. Karst, M., Halpern, J. H., Bernateck, M. & Passie, T. The non-hallucinogen 2-bromo-lysergic acid diethylamide as preventative treatment for cluster headache: an open, non-randomized case series. *Cephalalgia* **30**, 1140–1144 (2010).
10. McClure-Begley, T. D. & Roth, B. L. The promises and perils of psychedelic pharmacology for psychiatry. *Nat. Rev. Drug Discov.* **21**, 463–473 (2022).
11. Nichols, D. E. Psychedelics. *Pharmacol. Rev.* **68**, 264–355 (2016).
12. Glennon, R. A., Titeler, M. & McKenney, J. D. Evidence for 5-HT2 involvement in the mechanism of action of hallucinogenic agents. *Life Sci.* **35**, 2505–2511 (1984).
13. González-Maeso, J. et al. Hallucinogens recruit specific cortical 5-HT(2A) receptor-mediated signaling pathways to affect behavior. *Neuron* **53**, 439–452 (2007).
14. Titeler, M., Lyon, R. A. & Glennon, R. A. Radioligand binding evidence implicates the brain 5-HT2 receptor as a site of action for LSD and phenylisopropylamine hallucinogens. *Psychopharmacology* **94**, 213–216 (1988).
15. Preller, K. H. et al. Changes in global and thalamic brain connectivity in LSD-induced altered states of consciousness are attributable to the 5-HT2A receptor. *ELife* **7**, https://doi.org/10.7554/elife.35082 (2018).
16. Wallach, J. et al. Identification of 5-HT2A receptor signaling pathways associated with psychedelic potential. *Nat. Commun.* **14**, 8221 (2023).
17. Jones, K. A. et al. Rapid modulation of spine morphology by the 5-HT2A serotonin receptor through kalirin-7 signaling. *Proc. Natl. Acad. Sci. USA* **106**, 19575–19580 (2009).
18. Raval, N. R. et al. A single dose of psilocybin increases synaptic density and decreases 5-HT2A receptor density in the pig brain. *Int. J. Mol. Sci.* **22**, https://doi.org/10.3390/ijms22020835 (2021).
19. Willins, D. L., Deutch, A. Y. & Roth, B. L. Serotonin 5-HT2A receptors are expressed on pyramidal cells and interneurons in the rat cortex. *Synapse* **27**, 79–82 (1997).
20. Kim, K. et al. Structure of a hallucinogen-activated Gq-coupled 5-HT2A serotonin receptor. *Cell* **182**, 1574–1588.e19 (2020).
21. Cao, D. et al. Structure-based discovery of nonhallucinogenic psychedelic analogs. *Science* **375**, 403–411 (2022).
22. Nichols, D. E. Chemistry and structure-activity relationships of psychedelics. *Curr. Top. Behav. Neurosci.* **36**, 1–43 (2018).
23. Cao, C. et al. Structure, function and pharmacology of human itch GPCRs. *Nature* **600**, 170–175 (2021).

24. Lyu, J. et al. AlphaFold2 structures guide prospective ligand discovery. *Science* **384**, eadn6354 (2024).
25. Robertson, M. J., van Zundert, G. C. P., Borrelli, K. & Skiniotis, G. GemSpot: A pipeline for robust modeling of ligands into cryo-EM maps. *Structure* **28**, 707–716.e3 (2020).
26. Xu, P. et al. Structural insights into the lipid and ligand regulation of serotonin receptors. *Nature* **592**, 469–473 (2021).
27. Wacker, D. et al. Crystal structure of an LSD-bound human serotonin receptor. *Cell* **168**, 377–389 (2017).
28. Gumpper, R. H., Fay, J. F. & Roth, B. L. Molecular insights into the regulation of constitutive activity by RNA editing of 5HT2C serotonin receptors. *Cell Rep.* **40**, 111211 (2022).
29. Kaplan, A. L. et al. Bespoke library docking for 5-HT2A receptor agonists with antidepressant activity. *Nature* **610**, 582–591 (2022).
30. Turner, W. J., Almudevar, M. & Merlis, S. Chemotherapeutic trials in psychosis. III. Addendum-2-brom-d-lysergic acid diethylamide (BOL). *Am. J. Psychiatry* **116**, 261–262 (1959).
31. Lewis, V. et al. A non-hallucinogenic LSD analog with therapeutic potential for mood disorders. *Cell Rep.* **42**, 112203 (2023).
32. Cao, C. et al. Signaling snapshots of 5-HT2BR activated by theprototypical psychedelic LSD. *Neuron* **110**, 3154–3167 (2022).
33. Che, T. et al. Nanobody-enabled monitoring of kappa opioid receptor states. *Nat. Commun.* **11**, 1145 (2020).
34. Kimura, K. T. et al. Structures of the 5-HT2A receptor in complex with the antipsychotics risperidone and zotepine. *Nat. Struct. Mol. Biol.* **26**, 121–128 (2019).
35. Dror, R. O. et al. Activation mechanism of the β2-adrenergic receptor. *Proc. Natl. Acad. Sci. USA* **108**, 18684–18689 (2011).
36. Kato, H. E. et al. Conformational transitions of a neurotensin receptor 1-Gi1 complex. *Nature* **572**, 80–85 (2019).
37. Gumpper, R. H., Fay, J. & Roth, B. L. Molecular insights into RNA editing-induced regulation of serotoninergic signaling. *Cell Rep.* **40**, https://doi.org/10.1016/j.celrep.2022.111211 (2022).
38. Zhang, S. et al. Inactive and active state structures template selective tools for the human 5-HT5A receptor. *Nat. Struct. Mol. Biol.* **29**, 677–687 (2022).
39. White, K. L. et al. Identification of novel functionally selective κ-opioid receptor scaffolds. *Mol. Pharmacol.* **85**, 83–90 (2014).
40. Kenakin, T., Watson, C., Muniz-Medina, V., Christopoulos, A. & Novick, S. A simple method for quantifying functional selectivity and agonist bias. *ACS Chem. Neurosci.* **3**, 193–203 (2012).
41. Kenakin, T. & Christopoulos, A. Signalling bias in new drug discovery: detection, quantification and therapeutic impact. *Nat. Rev. Drug Discov.* **12**, 205–216 (2013).
42. Klein Herenbrink, C. et al. The role of kinetic context in apparent biased agonism at GPCRs. *Nat. Commun.* **7**, 10842 (2016).
43. Punjani, A. & Fleet, D. J. 3D variability analysis: Resolving continuous flexibility and discrete heterogeneity from single particle cryo-EM. *J. Struct. Biol.* **213**, 107702 (2021).
44. Punjani, A. & Fleet, D. J. 3DFlex: determining structure and motion of flexible proteins from cryo-EM. *Nat. Methods* **20**, 860–870 (2023).
45. Afonine, P. V. et al. Towards automated crystallographic structure refinement with phenix.refine. *Acta Crystallogr. D Biol. Crystallogr.* **68**, 352–367 (2012).
46. Lim, H. S. & Qiu, P. Quantifying cell-type-specific differences of single-cell datasets using uniform manifold approximation and projection for dimension reduction and shapley additive exPlanations. *J. Comput. Biol.* **30**, 738–750 (2023).
47. Koehl, A. et al. Structure of the μ-opioid receptor-Gi protein complex. *Nature* **558**, 547–552 (2018).
48. Mastronarde, D. N. Automated electron microscope tomography using robust prediction of specimen movements. *J. Struct. Biol.* **152**, 36–51 (2005).
49. Punjani, A., Rubinstein, J. L., Fleet, D. J. & Brubaker, M. A. cryoSPARC: algorithms for rapid unsupervised cryo-EM structure determination. *Nat. Methods* **14**, 290–296 (2017).
50. Punjani, A., Zhang, H. & Fleet, D. J. Non-uniform refinement: adaptive regularization improves single-particle cryo-EM reconstruction. *Nat. Methods* **17**, 1214–1221 (2020).
51. Bepler, T., Kelley, K., Noble, A. J. & Berger, B. Topaz-Denoise: general deep denoising models for cryoEM and cryoET. *Nat. Commun.* **11**, 5208 (2020).
52. Rosenthal, P. B. & Henderson, R. Optimal determination of particle orientation, absolute hand, and contrast loss in single-particle electron cryomicroscopy. *J. Mol. Biol.* **333**, 721–745 (2003).
53. Scheres, S. H. W. & Chen, S. Prevention of overfitting in cryo-EM structure determination. *Nat. Methods* **9**, 853–854 (2012).
54. Liebschner, D. et al. Macromolecular structure determination using X-rays, neutrons and electrons: recent developments in Phenix. *Acta Crystallogr. D Struct. Biol.* **75**, 861–877 (2019).
55. Afonine, P. V. et al. New tools for the analysis and validation of cryo-EM maps and atomic models. *Acta Crystallogr. D Struct. Biol.* **74**, 814–840 (2018).
56. Williams, C. J. et al. MolProbity: more and better reference data for improved all-atom structure validation. *Protein Sci* **27**, 293–315 (2018).
57. Sanchez-Garcia, R., Gomez-Blanco, J. & Cuervo, A. DeepEMhancer: a deep learning solution for cryo-EM volume post-processing. *Commun. Biol.* **4**, 874 (2020).
58. Pettersen, E. F. et al. UCSF ChimeraX: structure visualization for researchers, educators, and developers. *Protein Sci.* **30**, 70–82 (2021).
59. Emsley, P., Lohkamp, B., Scott, W. G. & Cowtan, K. Features and development of Coot. *Acta Crystallogr. D Biol. Crystallogr.* **66**, 486–501 (2010).
60. Croll, T. I. ISOLDE: a physically realistic environment for model building into low-resolution electron-density maps. *Acta Crystallogr. D Struct. Biol.* **74**, 519–530 (2018).
61. Moriarty, N. W., Grosse-Kunstleve, R. W. & Adams, P. D. Electronic ligand builder and optimization workbench (eLBOW): a tool for ligand coordinate and restraint generation. *Acta Crystallogr. D Biol. Crystallogr.* **65**, 1074–1080 (2009).
62. Gowers, R. et al. Mdanalysis: A python package for the rapid analysis of molecular dynamics simulations. In *Proceedings of the 15th Python in Science Conference* 98–105 (SciPy, 2016).
63. Olsen, R. H. J. et al. TRUPATH, an open-source biosensor platform for interrogating the GPCR transducerome. *Nat. Chem. Biol.* **16**, 841–849 (2020).

Acknowledgements

This work was supported by NIH grants RO1MH112205, R37DA045657, and the Defense Advanced Research Projects Agency HR0011-20-2-0029. The Titan X Pascal used for this research was kindly donated to J.F.F. by the NVIDIA Corporation. Also, we would like to thank the UNC cryo-EM facility, specifically Jared Peck and Dr. Joshua Strauss, for technical assistance using the Talos Arctica. B.L.R. and others in the Roth lab were also supported by the Michael Hooker Distinguished Professorship.

Author contributions

R.H.G. performed and planned the experiments in the paper, including cloning, BRET2, protein purification, cryo-EM, and subsequent analysis/modeling, and prepared and wrote the manuscript. M.K.J. helped prepare the manuscript and carried out the BRET1, BRET2 time course, and Nb6 kinetic studies. J.F.D. gathered the initial BRET data and time course. K.K. helped with the initial protein purification and complex solving as well as cloned the construct that was used to solve the structures. R.S., N.S., Z.X., H.U.K., and J.J. guided the medicinal chemistry efforts and synthesis of RS130-180 and also helped in the conceptualization of the

project. N.J.K. helped in gathering BRET data. B.E.K. helped with manuscript preparation and planning the experiments. D.E.N. guided structural analysis, proposed experiments, and helped prepare the manuscript. J.F. helped with all grid preparation, aided in data collection/processing of all the cryo-EM data, and helped prepare the manuscript. B.L.R. supervised and proposed the project, guided structural and functional studies, and prepared the manuscript.

Competing interests

R.H.G is an active consultant for 2A Biosciences. B.L.R. is a member of the SAB for Onsero, Escient, Septerna, Epiodyne, and Levator. J.J. is a cofounder and equity shareholder in Cullgen, Inc., a scientific cofounder and scientific advisory board member of Onsero Therapeutics, Inc., and a consultant for Cullgen, Inc., EpiCypher, Inc., Accent Therapeutics, Inc, and Tavotek Biotherapeutics, Inc. The Jin laboratory received or has received research funds from Celgene Corporation, Levo Therapeutics, Inc., Cullgen, Inc., and Cullinan Oncology, Inc. D.E.N. is a founder of 2A Biosciences. The remaining authors declare no competing interests.

Additional information

Supplementary information The online version contains supplementary material available at https://doi.org/10.1038/s41467-025-57956-7.

Correspondence and requests for materials should be addressed to Ryan H. Gumpper or Bryan L. Roth.

Peer review information *Nature Communications* thanks the anonymous reviewer(s) for their contribution to the peer review of this work. A peer review file is available.